

Improved numerical stability of stationary black hole evolution calculations

Hwei-Jang Yo^{1,2}, Thomas W. Baumgarte^{3,1}, and Stuart L. Shapiro^{1,4}

¹*Department of Physics, University of Illinois at Urbana-Champaign, Urbana, Illinois 61801*

²*Institute of Astronomy and Astrophysics, Academia Sinica, Taipei 115, Taiwan, Republic of China*

³*Department of Physics and Astronomy, Bowdoin College, Brunswick, Maine 04011 and*

⁴*Department of Astronomy & NCSA, University of Illinois at Urbana-Champaign, Urbana, Illinois 61801*

We experiment with modifications of the BSSN form of the Einstein field equations (a reformulation of the ADM equations) and demonstrate how these modifications affect the stability of numerical black hole evolution calculations. We use excision to evolve both non-rotating and rotating Kerr-Schild black holes in octant and equatorial symmetry, and without any symmetry assumptions, and obtain accurate and stable simulations for specific angular momenta J/M of up to about $0.9M$.

PACS numbers: 04.25.Dm, 04.30.Db, 95.30.Sf, 97.60.Lf

I. INTRODUCTION

Binary black holes are among the most promising sources for the gravitational wave laser interferometers currently under development, including LIGO, VIRGO, GEO, TAMA and LISA. The identification and interpretation of possible signals requires theoretically predicted gravitational wave templates. For the late epoch of the binary inspiral, numerical relativity is the most promising tool for the computation of such templates.

The numerical simulation even of single black holes has encountered numerous difficulties, which presumably arise from the complexity of Einstein's equations, the existence of a singularity inside the black hole, and the gauge (or coordinate) freedom inherent in general relativity. Some recent developments, however, have led to significant and very promising advances.

Traditionally, most numerical relativity simulations were based on the $3+1$ decomposition of Arnowitt, Deser and Misner (ADM, [1]), which has been shown to develop instabilities often [2, 3]. To avoid these instabilities, a number of hyperbolic formulations of Einstein's equations have been developed (see, e.g., [2, 4] as well as [5] and references therein). Alternatively, Shibata and Nakamura [6] and Baumgarte and Shapiro [3] introduced a modification of the original ADM equations that involves a conformal-traceless decomposition and the introduction of a new auxiliary variable (see Section II below). This formulation, now commonly referred to as the BSSN formulation, has led to significant improvements over the original ADM equations, and has been widely adopted (e.g. [7, 8, 9, 10, 11, 12]).

Singularities inside black holes were traditionally avoided by using "singularity avoiding" coordinate conditions, including maximal or polar slicing [13, 14, 15, 16]. Typically, these conditions lead to grid pathologies that cause codes to crash after relatively short times. An alternative strategy takes advantage of the fact that the black hole exterior is causally disconnected from the interior, so that a region of the black hole interior including the singularity can be excised from the computational grid. These "singularity excision" techniques

[17, 18, 19, 20, 21, 22] have led to large improvements in the simulation of single black holes, and are a promising tool for binary black hole evolutions (see [23] for preliminary results).

The application of singularity excision requires a coordinate system that is regular across black hole horizons, allowing smooth horizon penetration. For single black holes, one such coordinate system is the Kerr-Schild form, which can be used to represent both Schwarzschild and Kerr black holes (and which is also invariant under boosts). Binary black hole initial data based on Kerr-Schild coordinates can be constructed by solving the constraint equations of general relativity for "corrections" arising from superpositions of two boosted Kerr-Schild black holes [24, 25, 26, 27, 28].

Alcubierre and Brügmann [29] recently combined the BSSN formalism with a particularly simple singularity excision method to evolve single black holes in Kerr-Schild coordinates. Restricting the evolution to octant symmetry, all fields settle down to equilibrium (of the finite-difference equations), and no instabilities are encountered. If, however, the symmetry assumption is relaxed, instabilities develop and the code crashes after a few hundred M . Similar findings were reported in [30], where a completely independent formulation and implementation was adopted. Improvements over these results were discussed in [31, 32, 33], but even these do not completely eliminate the instabilities for evolutions without symmetry assumptions.

Recent results suggest that adding constraints to the evolution equations affects the numerical stability of the system (e.g. [33, 34, 35, 36, 37]; see [38] for an illustration in electrodynamics). In this paper we experiment with adding the new constraints that appear in the BSSN formulation to the evolution equation of the new auxiliary functions, and, following [37], the Hamiltonian constraint to the evolution equation for the spatial metric. We also experiment with schemes for imposing algebraic constraints on the conformally related metric and extrinsic curvature, as well as with different shapes for the excised region inside the black hole.

With these modifications we obtain evolutions of single black holes that last over several thousand M , indepen-

dent of any symmetry assumptions, without encountering any evidence of a growing instability. These findings hold both for static black holes and for rotating black holes with specific angular momentum of up to $0.9M$.

The paper is organized as follows: We summarize the BSSN formulation in Sec. II and black hole spacetimes in Kerr-Schild coordinates in Section III. Our modifications of the BSSN scheme are described in Sec. IV. In Section VI we present results of our simulations for both static and rotating BHs. We summarize and discuss the implications of our findings in Sec. VII. We also include an Appendix that explains our evaluation of the ADM mass and angular momentum. Throughout the paper we adopt geometrized units with $G = c = 1$.

II. THE BSSN FORMULATION

We write the metric in the ADM form

$$ds^2 = -\alpha^2 dt^2 + \gamma_{ij}(dx^i + \beta^i dt)(dx^j + \beta^j dt), \quad (1)$$

where α is the lapse function, β^i is the shift vector, and γ_{ij} is the spatial metric. Throughout this paper, Latin indices are spatial indices and run from 1 to 3, whereas Greek indices are space-time indices and run from 0 to 3.

The Einstein equations can then be decomposed into the Hamiltonian constraint \mathcal{H} and the momentum constraints \mathcal{M}_i

$$\mathcal{H} \equiv R - K_{ij}K^{ij} + K^2 = 0, \quad (2)$$

$$\mathcal{M}_i \equiv D_j K^j_i - D_i K = 0, \quad (3)$$

and the evolution equations

$$\frac{d}{dt}\gamma_{ij} = -2\alpha K_{ij}, \quad (4)$$

$$\frac{d}{dt}K_{ij} = -D_i D_j \alpha + \alpha(R_{ij} - 2K_{i\ell}K^\ell_j + K K_{ij}). \quad (5)$$

Here we have assumed vacuum $T_{\alpha\beta} = 0$ and have used

$$\frac{d}{dt} = \frac{\partial}{\partial t} - \mathcal{L}_\beta, \quad (6)$$

where \mathcal{L}_β is the Lie derivative with respect to β^i . D_i is the covariant derivative associated with γ_{ij} , R_{ij} is the three-dimensional Ricci tensor

$$R_{ij} = \frac{1}{2}\gamma^{k\ell}(\gamma_{kj,i\ell} + \gamma_{i\ell,kj} - \gamma_{k\ell,ij} - \gamma_{ij,k\ell}) + \gamma^{k\ell}(\Gamma^m_{i\ell}\Gamma_{mkj} - \Gamma^m_{ij}\Gamma_{mkl}), \quad (7)$$

and R is its trace $R = \gamma^{ij}R_{ij}$.

In the BSSN formalism [3, 6], the above ADM equations are rewritten by introducing the conformally related metric $\tilde{\gamma}_{ij}$

$$\tilde{\gamma}_{ij} = e^{-4\phi}\gamma_{ij}, \quad (8)$$

with the conformal factor chosen so that the determinant $\tilde{\gamma}$ of $\tilde{\gamma}_{ij}$ is unity

$$e^{4\phi} = \gamma^{1/3}. \quad (9)$$

The traceless part of the extrinsic curvature K_{ij} , defined by

$$A_{ij} = K_{ij} - \frac{1}{3}\gamma_{ij}K, \quad (10)$$

where $K = \gamma^{ij}K_{ij}$ is the trace of the extrinsic curvature, is conformally decomposed according to

$$\tilde{A}_{ij} = e^{-4\phi}A_{ij}. \quad (11)$$

The conformal connection functions $\tilde{\Gamma}^i$, initially defined as

$$\tilde{\Gamma}^i \equiv \tilde{\gamma}^{jk}\tilde{\Gamma}^i_{jk} = -\tilde{\gamma}^{ij}_{,j}, \quad (12)$$

are regarded as independent variables in this formulation.

The evolution equations of BSSN formulation can be written as

$$\frac{d}{dt}\phi = -\frac{1}{6}\alpha K, \quad (13)$$

$$\frac{d}{dt}\tilde{\gamma}_{ij} = -2\alpha\tilde{A}_{ij}, \quad (14)$$

$$\begin{aligned} \frac{d}{dt}K &= \alpha\left(\tilde{A}_{ij}\tilde{A}^{ij} + \frac{1}{3}K^2\right) - \gamma^{ij}D_i D_j \alpha \\ \frac{d}{dt}\tilde{A}_{ij} &= \alpha\left(K\tilde{A}_{ij} - 2\tilde{A}_{ik}\tilde{A}^k_j\right) \\ &\quad + e^{-4\phi}(\alpha R_{ij} - D_i D_j \alpha)^{TF}, \end{aligned} \quad (15)$$

$$\begin{aligned} \partial_t \tilde{\Gamma}^i &= 2\alpha\left(\tilde{\Gamma}^i_{jk}\tilde{A}^{jk} - \frac{2}{3}\tilde{\gamma}^{ij}K_{,j} + 6\tilde{A}^{ij}\phi_{,j}\right) \\ &\quad - 2\tilde{A}^{ij}\alpha_{,j} + \tilde{\gamma}^{jk}\beta^i_{,jk} + \frac{1}{3}\tilde{\gamma}^{ij}\beta^k_{,jk} + \beta^j\tilde{\Gamma}^i_{,j} \\ &\quad - \tilde{\Gamma}^j\beta^i_{,j} + \frac{2}{3}\tilde{\Gamma}^i\beta^j_{,j}. \end{aligned} \quad (16)$$

Here the superscript TF denotes the trace-free part of a tensor. The Ricci tensor R_{ij} can be written as a sum of two pieces

$$R_{ij} = \tilde{R}_{ij} + R_{ij}^\phi, \quad (17)$$

where R_{ij}^ϕ is given by

$$\begin{aligned} R_{ij}^\phi &= -2\tilde{D}_i\tilde{D}_j\phi - 2\tilde{\gamma}_{ij}\tilde{D}^k\tilde{D}_k\phi \\ &\quad + 4\tilde{D}_i\phi\tilde{D}_j\phi - 4\tilde{\gamma}_{ij}\tilde{D}^l\phi\tilde{D}_l\phi, \end{aligned} \quad (18)$$

while, with the help of the $\tilde{\Gamma}^i$, \tilde{R}_{ij} can be expressed as

$$\begin{aligned} \tilde{R}_{ij} &= -\frac{1}{2}\tilde{\gamma}^{mn}\tilde{\gamma}_{ij,mn} + \tilde{\gamma}_{k(i}\tilde{\Gamma}^k_{,j)} + \tilde{\Gamma}^k\tilde{\Gamma}_{(ij)k} \\ &\quad + \tilde{\gamma}^{mn}\left(2\tilde{\Gamma}^k_{m(i}\tilde{\Gamma}_{j)kn} + \tilde{\Gamma}^k_{in}\tilde{\Gamma}_{kmj}\right). \end{aligned} \quad (19)$$

The new variables are tensor densities, so that their Lie derivatives are

$$\mathcal{L}_\beta \phi = \beta^k \phi_{,k} + \frac{1}{6} \beta^k_{,k}, \quad (20)$$

$$\mathcal{L}_\beta \tilde{\gamma}_{ij} = \beta^k \tilde{\gamma}_{ij,k} + 2\tilde{\gamma}_{k(i} \beta^k_{,j)} - \frac{2}{3} \tilde{\gamma}_{ij} \beta^k_{,k}, \quad (21)$$

$$\mathcal{L}_\beta K = \beta^k K_{,k}, \quad (22)$$

$$\mathcal{L}_\beta \tilde{A}_{ij} = \beta^k \tilde{A}_{ij,k} + 2\tilde{A}_{k(i} \beta^k_{,j)} - \frac{2}{3} \tilde{A}_{ij} \beta^k_{,k}. \quad (23)$$

The Hamiltonian and momentum constraints (2) and (3) can be rewritten as

$$\begin{aligned} \mathcal{H} = e^{-4\phi} \left(\tilde{R} - 8\tilde{D}^i \tilde{D}_i \phi - 8\tilde{D}^i \phi \tilde{D}_i \phi \right) \\ + \frac{2}{3} K^2 - \tilde{A}_{ij} \tilde{A}^{ij} = 0 \end{aligned} \quad (24)$$

$$\mathcal{M}^i = \tilde{D}_j \tilde{A}^{ij} + 6\tilde{A}^{ij} \phi_{,j} - \frac{2}{3} \tilde{\gamma}^{ij} K_{,j} = 0, \quad (25)$$

where $\tilde{R} = \tilde{\gamma}^{ij} \tilde{R}_{ij}$.

III. BLACK HOLES IN KERR-SCHILD COORDINATES

The ingoing Kerr-Schild form of the Kerr metric is given by [24, 39]

$$ds^2 = (\eta_{\mu\nu} + 2H\ell_\mu \ell_\nu) dx^\mu dx^\nu, \quad (26)$$

where $\eta_{\mu\nu} = \text{diag}(-1, 1, 1, 1)$ is the Minkowski metric in Cartesian coordinates, and H a scalar function. The vector ℓ_μ is null both with respect to $\eta_{\mu\nu}$ and $g_{\mu\nu}$,

$$\eta^{\mu\nu} \ell_\mu \ell_\nu = g^{\mu\nu} \ell_\mu \ell_\nu = 0, \quad (27)$$

and we have $\ell_t^2 = \ell^i \ell_i$. The general Kerr-Schild BH metric has

$$H = \frac{Mr}{r^2 + a^2 \cos^2 \theta} \quad (28)$$

and

$$\ell_\mu = \left(1, \frac{rx + ay}{r^2 + a^2}, \frac{ry - ax}{r^2 + a^2}, \frac{z}{r} \right). \quad (29)$$

Here M is the mass of the Kerr BH, $a = J/M$ is the specific angular momentum of the BH, and r and θ are auxiliary spheroidal coordinates defined in terms of the Cartesian coordinates by

$$\frac{x^2 + y^2}{r^2 + a^2} + \frac{z^2}{r^2} = 1 \quad (30)$$

and $z = r \cos \theta$. The event horizon of the BH is located at

$$r_{\text{eh}} = M + \sqrt{M^2 - a^2}. \quad (31)$$

Comparing (26) with the ADM metric (1) one identifies the lapse function α , shift vector β_i and the spatial 3-metric γ_{ij} as

$$\alpha = (1 + 2H)^{-1/2}, \quad (32)$$

$$\beta_i = 2H\ell_i, \quad (33)$$

$$\gamma_{ij} = \eta_{ij} + 2H\ell_i \ell_j. \quad (34)$$

We can see here that these variables all extend smoothly through the horizon and their gradients near the horizon are well-behaved.. Given these metric quantities, the extrinsic curvature K_{ij} can be computed from (4)

$$\begin{aligned} K_{ij} = 2\alpha H \ell^k (\ell_i \ell_j H_{,k} + 2H \ell_{(i} \partial_k \ell_{j)}) \\ + 2\alpha (\ell_{(i} \partial_{j)} H + H \partial_{(i} \ell_{j)}), \end{aligned} \quad (35)$$

$$K = 2\alpha^3 (1 + H) \ell^i H_{,i} + 2\alpha H \ell^i_{,i}. \quad (36)$$

In the static case $a = 0$, the above expressions reduce to the Schwarzschild expressions in in-going Eddington-Finkelstein form [40]

$$\begin{aligned} H &= M/r, \\ \ell_\mu &= (1, x_i/r), \\ K_{ij} &= \frac{2M}{r^4 (1 + 2M/r)^{1/2}} \left[r^2 \eta_{ij} - (2 + \frac{M}{r}) x_i x_j \right] \\ K &= \frac{2M}{r^2 (1 + 2M/r)^{3/2}} (1 + 3M/r). \end{aligned} \quad (37)$$

where M is the total mass-energy and $r^2 = x^2 + y^2 + z^2$.

IV. ADJUSTING THE BSSN EQUATIONS

For a solution of the BSSN equations to be equivalent with a solution of the ADM equations, the new auxiliary variables have to satisfy new constraint equations. In particular, \tilde{A}_{ij} has to be traceless

$$\mathcal{A} \equiv \tilde{\gamma}^{ij} \tilde{A}_{ij} = 0, \quad (38)$$

the determinant of the conformally related metric $\tilde{\gamma}_{ij}$ has to be unity

$$\mathcal{D} \equiv \det(\tilde{\gamma}_{ij}) - 1 = 0, \quad (39)$$

and the conformal connection functions $\tilde{\Gamma}^i$ have to satisfy the identity (12)

$$\mathcal{G}^i \equiv \tilde{\Gamma}^i - \tilde{\gamma}^{jk} \tilde{\Gamma}^i_{jk} = 0. \quad (40)$$

These conditions can be viewed as new constraints, in addition to the Hamiltonian and momentum constraints (24) and (25).

In an unconstrained evolution calculation, the constraints are monitored only as a code check. It may be advantageous, however, either to enforce at least some of the constraints during the evolution, or to add evolution constraint equations to the evolution equations.

Alcubierre and Brügmann [29], for example, found improved stability properties when the algebraic constraint (38) is enforced. This can be achieved by replacing \tilde{A}_{ij} with

$$\text{AB1: } \tilde{A}_{ij} \leftarrow \tilde{A}_{ij} - \frac{1}{3}\tilde{\gamma}_{ij}\tilde{\gamma}^{mn}\tilde{A}_{mn} \quad (41)$$

after each time step. They also found improvements, at least in octant symmetry, when using the conformal connection function $\tilde{\Gamma}^i$ only in places where it is differentiated, and instead use, by virtue of (40), the contraction of the Christoffel symbols everywhere else

$$\text{AB2: } \tilde{\Gamma}^i \leftarrow \tilde{\gamma}^{jk}\tilde{\Gamma}_{jk}^i. \quad (42)$$

Other ways of imposing some of the constraints are possible (compare [31]). While the rule AB1 (equation 41) is appealing in that it treats all components of \tilde{A}_{ij} identically, we found particularly stable results by dynamically evolving only five of the six components of \tilde{A}_{ij} , and computing the zz component using the algebraic constraint (38)

$$\tilde{A}_{zz} = -\frac{\tilde{A}_x^x + \tilde{A}_y^y + \tilde{A}_{xz}\tilde{\gamma}^{xz} + \tilde{A}_{yz}\tilde{\gamma}^{yz}}{\tilde{\gamma}^{zz}}. \quad (43)$$

We similarly determine $\tilde{\gamma}_{zz}$ from the other five metric components using the algebraic constraint (39)

$$\tilde{\gamma}_{zz} = 1 + \frac{\tilde{\gamma}_{yy}\tilde{\gamma}_{xz}^2 - 2\tilde{\gamma}_{xy}\tilde{\gamma}_{yz}\tilde{\gamma}_{xz} + \tilde{\gamma}_{xx}\tilde{\gamma}_{yz}^2}{\tilde{\gamma}_{xx}\tilde{\gamma}_{yy} - \tilde{\gamma}_{xy}^2}. \quad (44)$$

In all our simulations, we use these two identities instead of rule AB1.

Combining (43) and (44) with rule AB2 leads to exponentially growing, unstable modes if no symmetry assumption is used. While it is not clear what exactly causes this instability in the absence of symmetry assumptions, one possible source is the last term in the evolution equation (16) for $\tilde{\Gamma}^i$, $(2/3)\tilde{\Gamma}^i\beta^j_{,j}$. If $\beta^j_{,j} > 0$, as for example for single black holes in Kerr-Schild coordinates, then this term may lead to exponential growth of any numerical error in $\tilde{\Gamma}^i$ (compare a similar discussion in [31]). The sign of this term can be reversed by adding a multiple of the product $\mathcal{G}^i\beta^j_{,j}$ to the evolution equation (16), specifically

$$\begin{aligned} \partial_t \tilde{\Gamma}^i &= \text{rhs of (16)} - \left(\chi + \frac{2}{3}\right) \mathcal{G}^i \beta^j_{,j} \\ &= 2\alpha \left(\tilde{\Gamma}_{jk}^i \tilde{A}^{jk} - \frac{2}{3} \tilde{\gamma}^{ij} K_{,j} + 6 \tilde{A}^{ij} \phi_{,j} \right) - 2 \tilde{A}^{ij} \alpha_{,j} \\ &\quad + \tilde{\gamma}^{jk} \beta^i_{,jk} + \frac{1}{3} \tilde{\gamma}^{ij} \beta^j_{,jk} + \beta^j \tilde{\Gamma}^i_{,j} - \tilde{\Gamma}^j \beta^i_{,j} \\ &\quad + \left[\left(\chi + \frac{2}{3} \right) \tilde{\gamma}^{kl} \tilde{\Gamma}^i_{kl} - \chi \tilde{\Gamma}^i \right] \beta^j_{,j}. \end{aligned} \quad (45)$$

Here χ is a free parameter, which in principle can even be chosen dynamically during an evolution calculation.

To suppress exponential growth of $\tilde{\Gamma}^i$, χ should have the same sign as $\beta^j_{,j}$.

For sufficiently slowly rotating black holes ($J/M \lesssim 0.7M$), we were able to follow the evolution for thousands of M without encountering any instabilities (see Section VI and Table I). For more rapidly rotating black holes ($J/M \sim 0.9M$) we experimented with adjustments suggested by Yoneda and Shinkai [37], namely

$$\frac{d}{dt} \tilde{\gamma}_{ij} = \text{rhs of (14)} - \kappa_1 \alpha \mathcal{H} \tilde{\gamma}_{ij} \quad (46)$$

and

$$\frac{d}{dt} \tilde{A}_{ij} = \text{rhs of (15)} - \kappa_2 \alpha e^{-4\phi} \tilde{\gamma}_{ij} \mathcal{G}^k_{,k}, \quad (47)$$

where κ_1 and κ_2 are positive numbers. We did find improvements with the adjustment (46), but not with (47) (see Table I).

V. NUMERICAL IMPLEMENTATION

Our numerical implementation follows very closely the recipe suggested by Alcubierre and Brügmann [29]. We finite-difference the evolution equations using an iterative Crank-Nicholson scheme with two corrector steps [41].

We use centered differencing everywhere except for the advection terms on the shift (terms involving $\beta^i \partial_i$). For these terms, a second-order upwind scheme is used along the shift direction.

We adopt “1+log” slicing [42, 43, 44]

$$\partial_t \alpha = D_i \beta^i - \alpha K \quad (48)$$

to specify the lapse α . The shift β^i is determined either from the analytic solution, or from the “Gamma-driver” condition

$$\partial_t \beta^i = \lambda \partial_t \tilde{\Gamma}^i \quad (49)$$

(see [29]), where we choose $\lambda = 0.05$ in our simulations [45].

On the outer boundaries of the numerical grid we impose a radiative boundary condition that is imposed on the difference between a given variable and its analytic value $f - f_{\text{analytic}} = u(r - t)/r$ where u is an outgoing wave function. We apply this condition to all fields except $\tilde{\Gamma}^i$ which we leave fixed to their analytic values at the boundary.

We experiment with both cubic and spherical excision regions. For cubical excision regions, we adopt the recipe suggested by [29] to copy the time derivative of every field at the boundary from its value on a neighboring grid-point. For surfaces, we copy from the nearest grid-point along the outward normal, and for edges and corners from the nearest grid-point along the corresponding diagonal.

A generalization of this copying algorithm for spherical excision methods has been suggested in [46]. For

TABLE I: Input parameters for selected evolutions. For each evolution we list the lapse condition, the shift condition, the symmetry used, the parameter χ in equation (45), the parameter κ_1 in equation (46), the excision shape, the time when the changes in all the variables reach the level of round-off error (if achieved), and the total run time.

Case ^a	J/M	Lapse	Shift ^b	Symmetry ^c	χ ^d	κ_1	excision	Machine accuracy ^e	Run time ^f
O0	0	Ana	Ana	Oct	AB2	0	cube	No	$< 100M$
O1	0	1 + log	Ana	Oct	AB2	0	cube	1200M	$> 2000M$
O2	0	1 + log	Γ	Oct	AB2	0	cube	1000M	$> 2000M$
O3	0	1 + log	Ana	Oct	0	0	cube	1800M	$> 3000M$
O4	0	1 + log	Γ	Oct	0	0	cube	1200M	$> 2000M$
O5	0	1 + log	Ana	Oct	0	0	sphere	2200M	$> 3000M$
O6	0	1 + log	Ana	Oct	1/3	0	cube	1600M	$> 2000M$
E0	0	1 + log	Ana	Equ	AB2	0	cube	No	1900M
E1	0	1 + log	Ana	Equ	0	0	cube	1800M	$> 4000M$
E2	0	1 + log	Γ	Equ	0	0	cube	1200M	$> 3000M$
E3	0	1 + log	Ana	Equ	1/3	0	cube	1600M	$> 3000M$
E4	0	1 + log	Ana	Equ	1/3	0	sphere	No	$< 200M$
E5	0	1 + log	Ana	Equ	3/4	0	sphere	1400M	$> 2200M$
N1	0	1 + log	Ana	None	2/3	0	cube	1500M	$> 3000M$
N2	0	1 + log	Γ	None	2/3	0	cube	1000M	$> 2000M$
N3	0	1 + log	Γ	None	2/3	0	cube	700M	$> 1000M$
N4	0	1 + log	Γ	None	2/3	0	cube	500M	$> 1000M$
A1	0.7M	1 + log	Ana	Equ	1/3	0	cube	3000M	$> 4000M$
A2	0.7M	1 + log	Γ	Equ	1/3	0	cube	2000M	$> 3500M$
A3	0.9M	1 + log	Ana	Equ	1/3	0	cube	No	$> 1000M$
A4	0.9M	1 + log	Ana	Equ	2/3	0	cube	No	$> 3200M$
A5	0.9M	1 + log	Ana	Equ	2/3	0.1	cube	—	$> 3300M$
A6	0.9M	1 + log	Ana	Equ	2/3	0.2	cube	—	$> 3400M$
A7	0.9M	1 + log	Γ	Equ	2/3	0	cube	—	$> 4600M$
A8	0.9M	1 + log	Γ	Equ	2/3	0.1	cube	4600M	$> 5700M$

^aCases N3 and N4 have smaller domains; case N4 uses a smaller grid spacing (see text).

^bAna, analytic; Γ : Gamma driver (Eq. 49).

^cOct, octant; Equ, equatorial.

^dAB2, adopting rule AB2 (Eq. 42) instead of using Eq. (45).

^eFor the symbol “—” see Fig. 10.

^fThe symbol “>” means the run is terminated at this time but could continue.

a boundary grid-point (i, j, k) of the excised sphere we take its nearest neighbors along the coordinate axes away from the center of the BH, say $(i + 1, j, k)$, $(i, j + 1, k)$ and $(i, j, k + 1)$. These three points define a plane, and we interpolate to the intersection of this plane with the normal on the surface of the excised region. If one of these three neighbors is also a boundary grid-point, we project the normal into the line defined by the remaining two neighbor points, and do the interpolation there; if two of the neighbors are inside the excised region we directly copy the remaining third point. If all three points are inside the excised region we average the three diagonal points $(i + 1, j + 1, k)$, $(i + 1, j, k + 1)$ and $(i, j + 1, k + 1)$; if that is also not successful we finally copy the point $(i + 1, j + 1, k + 1)$.

We empirically find improved stability if copying along the x or y direction is given higher priority than copying along the z direction. This asymmetry is probably introduced by (43) and (44). We therefore use the grid-point $(i, j, k + 1)$ ($(i + 1, j, k + 1)$ and/or $(i, j + 1, k + 1)$)

only when the grid-points $(i + 1, j, k)$ and $(i, j + 1, k)$ ($(i + 1, j + 1, k)$) are not available.

VI. NUMERICAL RESULTS

Our simulations are summarized in Table I. For most of these simulations we use computational domains of size $0 < x, y, z < 12M$ for octant symmetry, $-12M < x, y < 12M$ and $0 < z < 12M$ for equatorial symmetry, and $-12M < x, y, z < 12M$ for no symmetry, with a grid spacing of $\Delta x = 0.4M$. In order to analyze the effect of resolution we also performed the two Cases N3 and N4 on a smaller domain of $-6M < x, y, z < 6M$ and used a resolution of $\Delta x = 0.4M$ for N3 and $\Delta x = 0.2M$ for N4. An additional simulation with a resolution of $\Delta x = 0.8M$ (not included in Table I) was used to establish second order convergence of our code in regions not influenced by the excision surface. We always use a Courant factor of 1/4 so that $\Delta t = \Delta x/4$. We excise cubes of volume

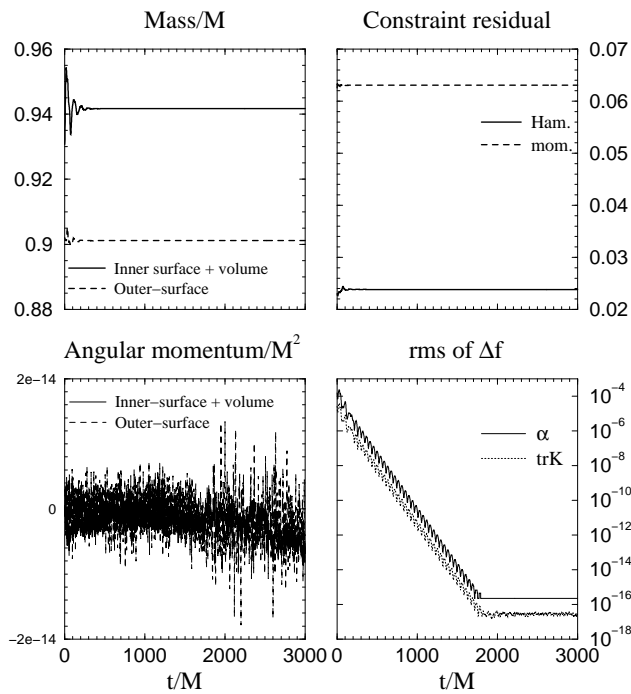


FIG. 1: The monitored quantities as functions of time for Case O3. The upper-left panel compares different integrals for the ADM mass. The solid line is obtained by using Eq. (A12); the dashed line is obtained by using rhs of Eq. (A11). The radius of the inner surface is $1.5M$ and the radius of the outer surface is $11.5M$. The lower-left panel compares different integrals for the angular momentum. The solid line is obtained by using Eq. (A20); the dashed line is obtained by using rhs of Eq. (A19). The upper-right panel shows the L_2 norms of the Hamiltonian constraint \mathcal{H} (the solid line) and the momentum constraint \mathcal{M}^x (the dashed line). The lower-right panel shows a log plot of the root mean square (r.m.s.) of the changes in the lapse (the solid line) and the trace of extrinsic curvature (the dotted line) between consecutive time steps.

$(1M)^3$ in octant symmetry, $(2M)^2 \times 1M$ in equatorial symmetry, and $(2M)^3$ without symmetry assumptions, or spheres of radius $1M$.

We will call a simulation “stable” if changes in dynamical variables ϕ , $\tilde{\gamma}_{ij}$, K , \tilde{A}_{ij} , $\tilde{\Gamma}^i$, α and β^i drop to round-off error (of about 10^{-16} in double-precision), and remain at that level for several hundred M . Reaching round-off implies that the numerical solution has settled down to the equilibrium solution of the finite-difference equations (as opposed to the equilibrium solution of the differential equations, which is provided as initial data). In all our stable runs, besides monitoring the global quantities consisting of the ADM mass, the angular momentum J_z , the L_2 norms of the Hamiltonian constraint \mathcal{H} , the momentum constraint \mathcal{M}^x , and the Gamma constraint \mathcal{G}^x violations, we also monitor the changes in the representative variables, i.e., ϕ , α , K , $\tilde{\gamma}_{xx}$, and \tilde{A}_{xx} , until they reach and remain at the level of round-off error. Once the equilibrium solution with a fixed resolution is achieved,

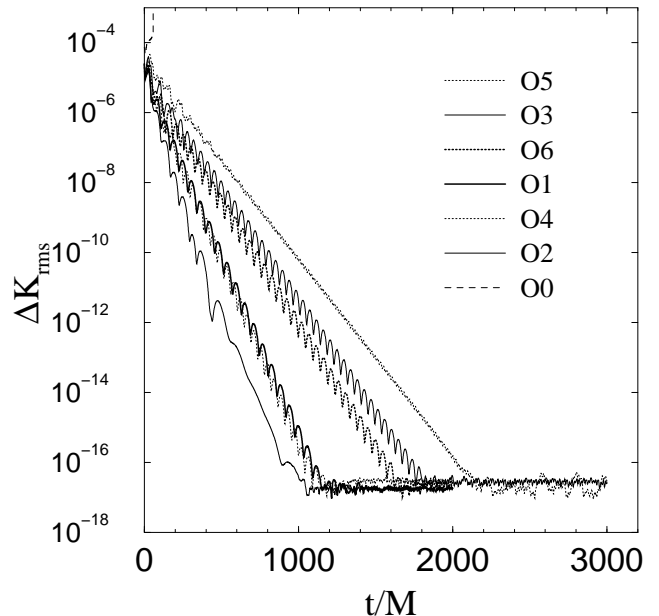


FIG. 2: The r.m.s. of the change in the trace of extrinsic curvature between consecutive time steps as functions of time in the static cases with octant symmetry. The lines are labeled sequentially from right to left. Case O0 uses an analytic lapse condition. Recipe AB2 is used in Cases O1 and O2, while the modification (45) is adopted in Cases O3 — O6. In Case O5 an excision sphere instead of a cube is used. All of these cases are stable and the K ’s all reach their equilibrium values except Case O0. Cases O3 and Case O6 are identical except that $\chi = 0$ was used in O3 and $\chi = 1/3$ in O6, illustrating the effect of the modification (45) in stability.

we never observe any instability growing up from the round-off error at later time.

In Table I we tabulate the time at which any run reaches equilibrium, and the time after which the simulation is terminated.

Simulations of non-rotating black holes are labeled “O” for octant symmetry, “E” for equatorial symmetry, and “N” for no symmetry.

A. Non-rotating Black Holes

We first compare several evolutions in octant symmetry. Cases O0 and O1 are identical except that in O0 the analytical lapse is used, while in O1 “1+log” slicing (48) is used. O0 crashes after a short time, while O1 is stable.

Cases O1 and O2 confirm that Alcubierre and Brügmann’s [29] algorithm (including their rule AB2) leads to stable evolution in octant symmetry, both for analytic shift and the “Gamma-driver” condition. The latter consistently allows the numerical solution to reach equilibrium in a shorter time than the former. Simulations O3 — O6 show that similar results can be obtained by replacing AB2 with the inclusion of the constraint in

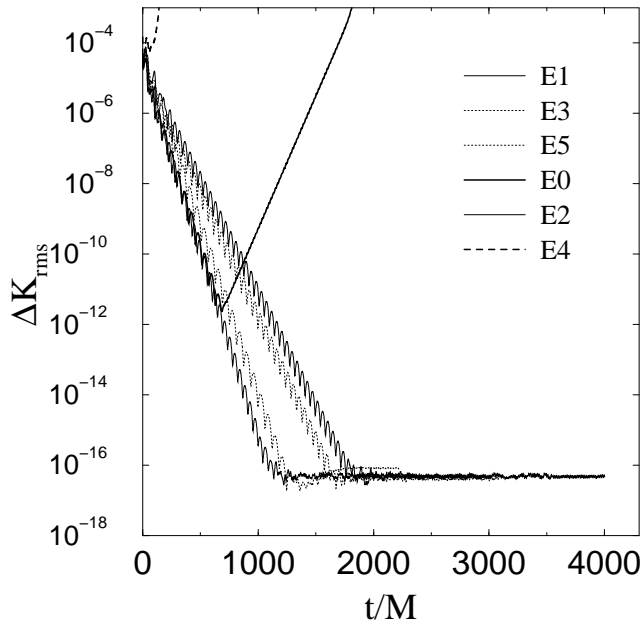


FIG. 3: The r.m.s. of the change in the trace of extrinsic curvature between consecutive time steps as functions of time in the static cases with equatorial symmetry. The lines are labeled sequentially from right to left. The recipe AB2 is used in Cases E0. The modification (45) is used in Cases E1 — E5 with different values of χ . In Case E4 and E5 an excision sphere instead of a cube is used. All of these cases are stable except Case E0 and E4. In E0 an instability appears at $t \sim 700M$ and the code crashes at $t \sim 1900M$. In E4 the code becomes unstable at the beginning and crashes at $t \sim 140M$.

equation (45). In Case O5 an excision sphere instead of a cube is used.

Results for case O3 are presented in Fig. 1. The upper-left panel shows two different integrations of the ADM masses which are derived in Appendix A 1 and illustrated in Fig. 11. The dashed line is computed from a surface integral at large separation (equation (A11)), while the solid line is computed from a volume integral plus a surface integral over a small sphere enclosing the black hole singularity (equation A12). We choose a radius of $R_1 = 1.5M$ for the inner surface and $R_2 = 11.5M$ for the outer surface. For $R_2 \rightarrow \infty$ the two mass integrals should agree and should yield the analytic value M of the initial data. Our two mass integrals agree to within about 5 %. Their difference arises both from the finite grid spacing, which generates greater error for surface integrals vs. volume integrals, as well as spurious effects near the outer boundary, which may more seriously affect the outer surface integral. Their deviation from unity is a measure of error induced by the proximity of the outer boundary to the black hole.

The lower-left panel in Fig. 1 shows surface and volume integrations of the angular momentum, similar to the mass integrations explained above (see Appendix A 2). The dashed line is computed from the outer surface in-

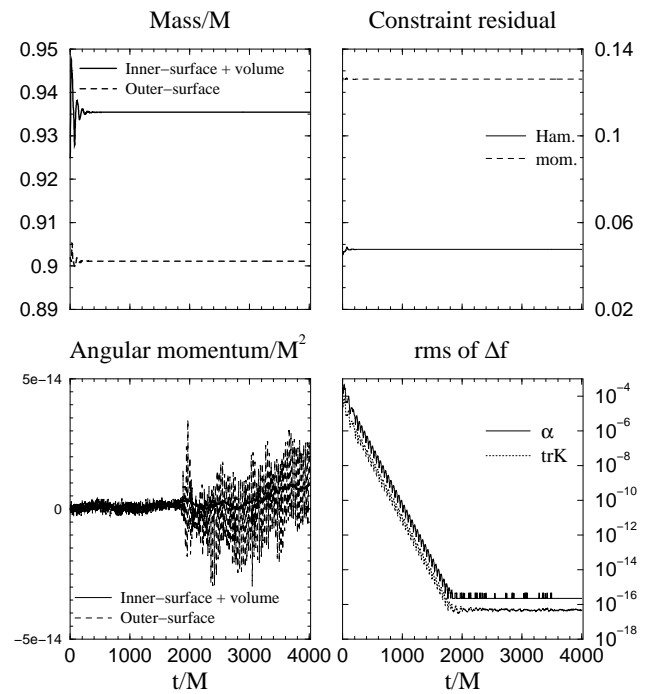


FIG. 4: The monitored quantities as functions of time for Case E1. Labeling is the same as in Fig. 1.

tegral (A19); the solid line is computed from a combination of volume integral and inner surface integral (see equation (A20)). For both integrations the angular momentum is very close to zero, as it is supposed to be.

The upper-right panel shows the L2 norms of the Hamiltonian constraint \mathcal{H} (solid line) and the momentum constraint \mathcal{M}^x (dashed line). The lower-right panel shows a log plot of the root mean square (r.m.s.) of the changes in the lapse α (the solid line) and the trace of extrinsic curvature K (the dashed line) between consecutive time steps. The changes in α and K both decrease as exponentially damped oscillations until they reach round-off error at about $t \sim 1800M$. Using the dynamical shift condition (49) expedites the damping of these changes and helps to stabilize the code (compare, for example, cases O1 and O2 or cases O3 and O4). In Fig. 2 we compare the r.m.s. of changes in K for all cases in octant symmetry.

Reconfirming the findings of [29], we were unable to obtain stable evolutions with method AB2 if the symmetry is relaxed from octant to equatorial. The result of such an evolution (E0) is included in Fig. 3, where we plot the r.m.s. changes of K for various different cases in equatorial symmetry. For the case E0, the changes again drop exponentially until $t \sim 700M$, but at later times they increase exponentially. This exponentially growing mode can be extrapolated back to about round-off error at $t = 0$, indicating that the mode is triggered by round-off error in the initial data. Using the Gamma-driver shift condition instead of the analytic shift leads to similarly

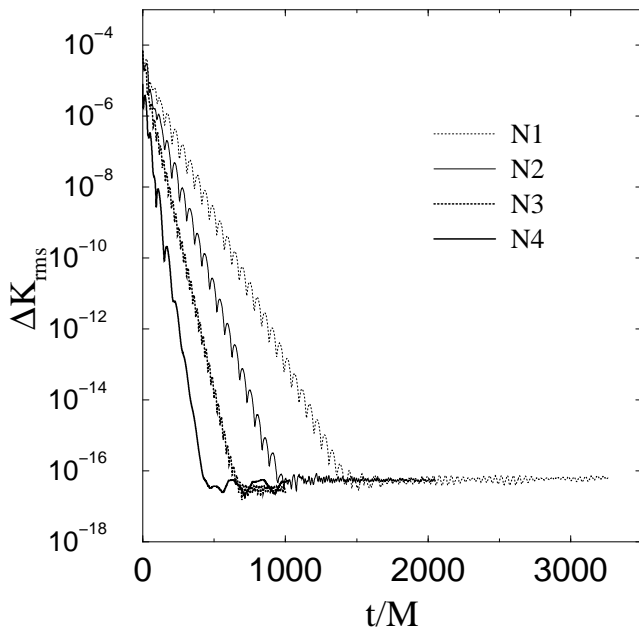


FIG. 5: The the r.m.s. of the change in the trace of extrinsic curvature between consecutive time steps as functions of time in the static cases with none symmetry. The lines are labeled sequentially from right to left. The settings of case N2 and N3 are the same except the computational domain of case N3 is half size of case N2 in length. The change of K of case N3 drops faster than in K of case N2 because that light cross time in case N3 is shorter than in case N2. The settings of Case N3 and N4 are the same except the resolution in case N4 is two times higher than in case N3.

unstable evolutions. However, replacing the method AB2 with our modification (45) with $\chi \geq 0$, we recover stable evolutions, in which all changes drop exponentially until they reach round-off error.

In Fig. 3 we compare several different cases in equatorial symmetry, analyzing the effect of the shift condition, the value of χ in (45), and the shape of the excised region. As before, we find that using the Gamma-condition instead of the analytic shift leads to a more rapid settling down to equilibrium, and comparing cases E1 and E3 shows that increasing χ has a similar effect. Comparing cases E3 and E4, we find that changing the excision shape from cubic to spherical with the other settings unchanged can destabilize the code, indicating that our copying method on an excised sphere leads to larger numerical error than on an excised cube. Stability can be restored by increasing the value of χ , as for case E5. Details for the case E1 are presented in Fig. 4.

We find that larger values of χ are needed to obtain long-term stable evolutions if symmetry assumptions are completely removed. In all cases with no symmetry $\chi = 2/3$ is used. We compare the results of these runs in Figure 5. The cases N2 and N3 are identical except that that the computational domain of N3 is half as large as that of N2. We find that N3 settles down to equilibrium

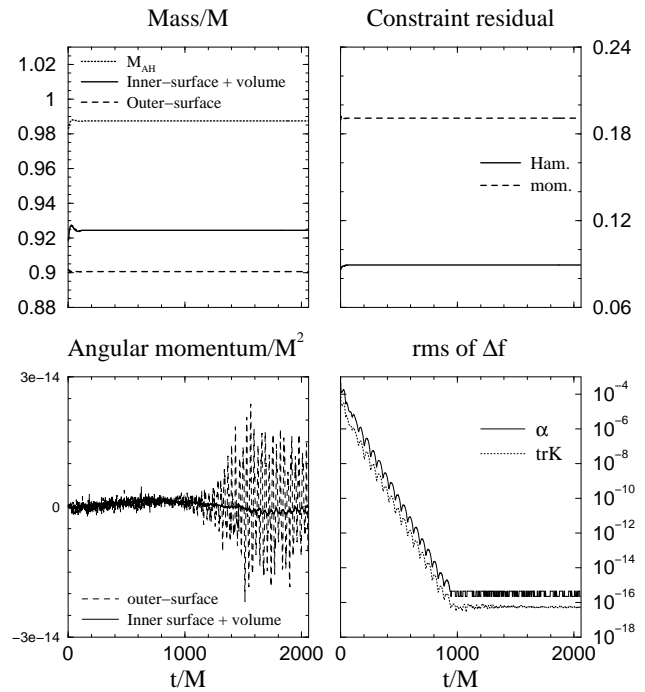


FIG. 6: The monitored quantities as functions of time for Case N2. Labeling is the same as in Fig. 1, except in the upper-left panel the dotted line is the apparent horizon mass.

faster than N2, which can be understood in terms of the shorter light crossing time. Similarly, cases N3 and N4 are identical except that N4 has twice the resolution of N3, leading to smaller errors and again faster approach to equilibrium.

Fig. 6 shows the result of case N2. In this evolution we also locate the apparent horizon every 20 time-steps using the 3D finder described in [47]. The apparent horizon mass $M_{AH} = (A/16\pi)^{1/2}$, computed from its area A , is included in the upper-left panel in Fig. 6 and agrees with the analytic value to within less than 2 %.

B. Rotating Black Holes

We now turn to black holes with non-zero angular momentum. Figure 7 shows the results of Case A1 with a moderate value of the specific angular momentum $a \equiv J/M = 0.7M$. Comparing with our results for non-rotating black holes we find that the constraint violations are larger, and that it takes a longer time for the solution to settle down to equilibrium ($t \sim 3000M$ for A1). The mass integrals have larger oscillations at early times than those for non-rotating black holes, but settle down to similar values as before. We also find that the values for the angular momentum settle down to values within about 2 % of the analytically correct ones. In Fig. 8 we compare the r.m.s. of changes in K for A1 and A2, which again demonstrates that the Gamma-driver

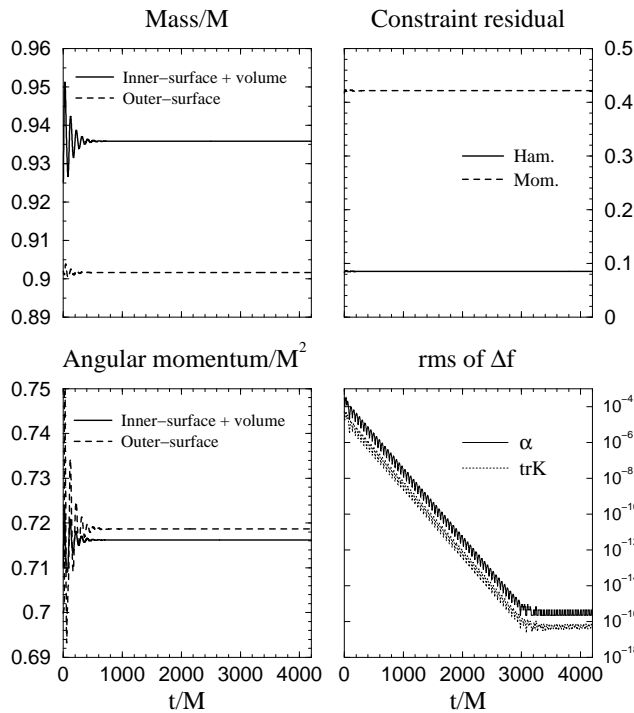


FIG. 7: The monitored quantities as functions of time for Case A1. Labeling is the same as in Fig. 1.

shift condition helps to stabilize the evolution.

Instabilities become even harder to control for $a = 0.9M$. The larger angular momentum leads to larger numerical error, which by itself makes the simulations more demanding. In addition, the event horizon for more rapidly rotating black holes is smaller. For $a = 0.7M$, our excision cube of physical side length $2M$ (corresponding to a volume of $(2M)^2 \times 1M$ in equatorial symmetry), just barely fits inside the event horizon. For $a = 0.9M$, we decreased the size of the excision cube to $(1.6M)^2 \times 0.8M$ so that it does not protrude from the event horizon. However, we were unable to obtain stable evolution with the reduced size of the excised region, which is probably caused by the increasingly large gradients of the gravitational fields close to the black hole's central singularity. Interestingly, we were able to obtain stable evolution when we left the excision surface at its original size of $(2M)^2 \times 1M$. This surface protrudes from the horizon by small amounts at the corners of the cube, which introduces errors into the solution. However, these errors occur very close to the horizon and hardly affect the solution in the asymptotic region at all.

In Fig. 10 we compare the r.m.s. of the change in K for different parameter settings. Case A3, in which the setting is the same as case A1 except increasing a from $0.7M$ to $0.9M$, shows an exponentially growing mode, indicating an instability. The unstable mode still cannot be suppressed in case A4 in which χ has been increased from $1/3$ to $2/3$. We find that this instability can be controlled by adding the Hamiltonian to the evolution

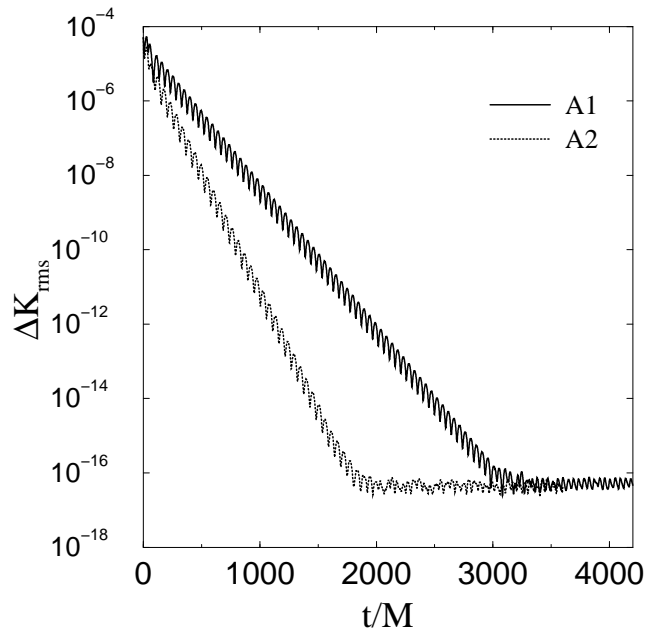


FIG. 8: The r.m.s. of the change in the trace of extrinsic curvature between consecutive time steps as functions of time in the rotating cases with $a = 0.7M$.

equation for the spatial metric (46) as suggested by [37] (cases A5 and A6). Changing from analytical shift to the Gamma-driver shift condition turns out to be more effective (case A7), and, not surprisingly, we find the fastest decay of changes in K by combining both methods (case A8). We show details of case A8 in Fig. 9.

VII. SUMMARY

We experiment with various modifications of the BSSN formulation and study their effect on the stability of numerical evolution calculations of static and rotating black holes. We force the determinant of the conformally related metric to be unity and the trace of the traceless part of the extrinsic curvature to be zero. We modify the evolution equation for the new auxiliary conformal connection functions by adding their constraint equation, and also experiment with adjustments of the other evolution equations suggested by [37].

Most importantly, we find that an instability that arises when octant symmetry is relaxed [29, 30, 31, 32, 33] can be overcome when the above modifications are employed. We demonstrate that both static and moderately rapidly rotating black holes can be evolved stably without encountering any growing modes. Any changes in grid functions settle down to round-off error and remain there for several $1000 M$.

We find that the dynamically enforced “Gamma-driver” spatial gauge condition for the shift leads to more stable evolution than using the analytical shift. We

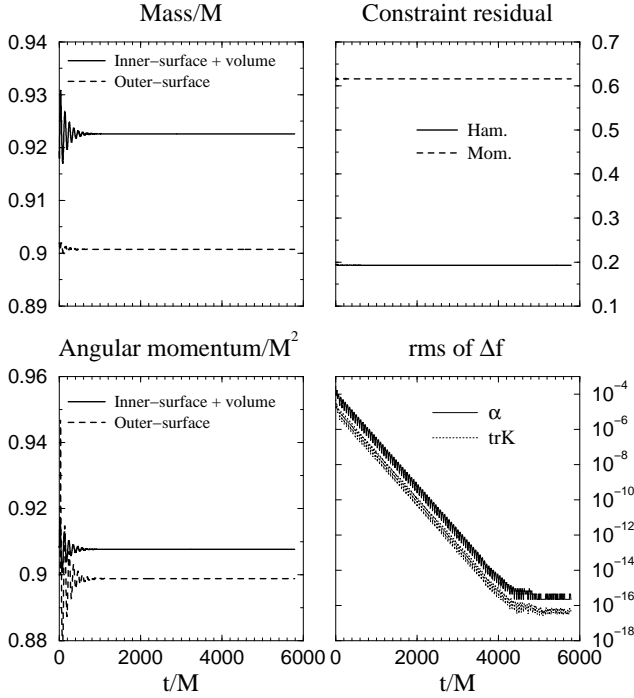


FIG. 9: The monitored quantities as functions of time for Case A7. Labeling is the same as in Fig. 1.

also find that cubical excision surfaces, which are more straight-forward to implement in Cartesian coordinates, work better than spherical excision surfaces.

While our modifications do not solve all stability problems (e.g. for the most extreme rapidly rotating black holes), we believe that they lead to significant improvements that may be a helpful step towards simulations of binary black holes and their coalescence.

Acknowledgments

It is a pleasure to thank Matthew Duez and Pedro Marronetti for helpful discussions. This work was supported in part by NSF Grants PHY 00-90310 and PHY-0205155, and NASA Grant NAG 5-10781 at the University of Illinois at Urbana-Champaign (UIUC), NSF Grant PHY 0139907 at Bowdoin College, and the National Science Council of the R.O.C. (Taiwan) under grant No. NSC90007P. Some of the calculations were performed at the National Center for Supercomputing Applications at UIUC. HJY acknowledges the support of the Academia Sinica, Taipei, Taiwan.

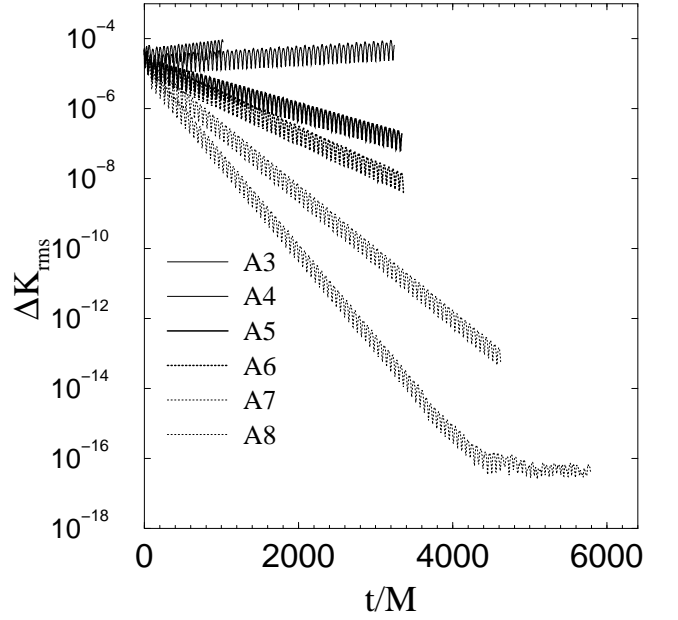


FIG. 10: The r.m.s. of the change in the trace of extrinsic curvature between consecutive time steps as functions of time in the rotating cases with $a = 0.9M$. The lines are labeled sequentially from up to down. The gradual rise of the ΔK_{rms} in Case A3 and A4 indicates an instability. The modification (46) is used and different values of κ are tested for stability in Cases A5 and A6. The Gamma-driver shift condition is used in both Cases A7 and A8, and the modification (46) is used in Case A8 with $\kappa = 0.1$. The improvement of stability can be seen in this figure by using these modifications.

APPENDIX A: EVALUATION OF THE ADM MASS AND ANGULAR MOMENTUM

1. ADM Mass Integration

The ADM mass is defined in terms of a surface integral at spatial infinity. In numerical simulations, this integral can be approximated by an integral evaluated on a surface near the outer boundaries of the grid ($\partial\Omega_2$ in Fig. 11). To avoid spurious effects of the outer boundaries, it is often desirable to convert this surface integral into a volume integral. For black hole spacetimes there is the additional complication of singularities in the black hole interiors. In this Appendix, we show how a region inside the grid can be excluded, so that the mass can be computed from a volume integral over the outer region and a surface integral over the boundary of excised interior regions.

In Cartesian coordinates, the ADM mass is defined by a surface integral at spatial infinity [48]

$$M = \frac{1}{16\pi} \oint_{\infty} \gamma^{im} \gamma^{jn} (\gamma_{mn,j} - \gamma_{jn,m}) dS_i. \quad (\text{A1})$$

where $dS_i \equiv (1/2) \gamma^{1/2} \epsilon_{ijk} dx^j dx^k$ is the surface element and ϵ_{ijk} the Levi-Civita alternating symbol. We now

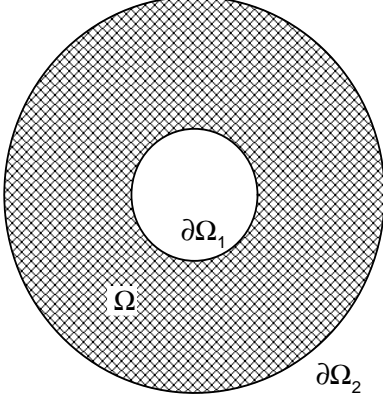


FIG. 11: The diagram illustrates the relation between the volume integral on the volume Ω and the surface integrals on the boundaries $\partial\Omega_1$ and $\partial\Omega_2$.

perform a conformal decomposition

$$\gamma_{ij} = \psi^4 \bar{\gamma}_{ij}. \quad (\text{A2})$$

where we distinguish from the decomposition (8) in order to allow for conformally related metrics $\bar{\gamma}_{ij}$ with a determinant different from unity. Assuming the asymptotic behavior

$$\psi \sim 1 + O\left(\frac{1}{r}\right) \quad \text{when} \quad r \rightarrow \infty \quad (\text{A3})$$

and

$$\bar{\gamma}_{ij} \sim \delta_{ij} + O\left(\frac{1}{r}\right) \quad \text{when} \quad r \rightarrow \infty, \quad (\text{A4})$$

we can rewrite (A1) as

$$\begin{aligned} M &= \frac{1}{16\pi} \oint_{\infty} \psi^{-2} \bar{\gamma}^{im} \bar{\gamma}^{jn} [\psi^4 (\bar{\gamma}_{mn,j} - \bar{\gamma}_{jn,m}) \\ &\quad + 4\psi^3 (\psi_{,j} \bar{\gamma}_{mn} - \psi_{,m} \bar{\gamma}_{jn})] d\bar{S}_i \\ &= \frac{1}{16\pi} \oint_{\infty} \bar{\gamma}^{im} [\bar{\gamma}^{jn} (\bar{\gamma}_{mn,j} - \bar{\gamma}_{jn,m}) - 8\psi_{,m}] d\bar{S}_i \\ &= \frac{1}{16\pi} \oint_{\infty} (\bar{\Gamma}^i - \bar{\Gamma}^{ji}{}_j) d\bar{S}_i - \frac{1}{2\pi} \oint_{\infty} \bar{D}^i \psi d\bar{S}_i. \end{aligned} \quad (\text{A5})$$

Here the conformal surface element is defined as $d\bar{S}_i = (1/2)\bar{\gamma}^{(1/2)}\epsilon_{ijk}dx^jdx^k$, we use the abbreviations $\bar{\Gamma}^i \equiv \bar{\gamma}^{jk}\bar{\Gamma}^i{}_{jk}$ and $\bar{\Gamma}^{ij}{}_k \equiv \bar{\gamma}^{jl}\bar{\Gamma}^i{}_{lk}$, and \bar{D}_i is the three-covariant derivative with respect to the metric $\bar{\gamma}_{ij}$.

Using Gauss' law, the surface integral (A5) can be converted into a volume integral. For spacetimes containing a black hole, we can exclude an interior region from the volume integration and write the integral over an outer surface $\partial\Omega_2$ as a sum of a volume integral over Ω and a surface integral over an inner surface $\partial\Omega_1$,

$$\int_{\partial\Omega_2} u^i d\bar{S}_i = \int_{\Omega} \partial_i (\sqrt{\bar{\gamma}} u^i) d^3x + \int_{\partial\Omega_1} u^i d\bar{S}_i \quad (\text{A6})$$

as illustrated in Fig. 11. For spacetimes with more than one black hole, several interior surfaces can be added on the right hand side.

Applying Gauss' law to the first term of the right hand side of equation (A5) yields

$$\begin{aligned} &\oint_{\partial\Omega_2} (\bar{\Gamma}^i - \bar{\Gamma}^{ji}{}_j) d\bar{S}_i \\ &= \oint_{\partial\Omega_1} (\bar{\Gamma}^i - \bar{\Gamma}^{ji}{}_j) d\bar{S}_i + \int_{\Omega} \partial_i [\sqrt{\bar{\gamma}} (\bar{\Gamma}^i - \bar{\Gamma}^{ji}{}_j)] d^3x \\ &= \oint_{\partial\Omega_1} (\bar{\Gamma}^i - \bar{\Gamma}^{ji}{}_j) d\bar{S}_i \\ &\quad + \int_{\Omega} [\partial_i (\bar{\Gamma}^i - \bar{\Gamma}^{ji}{}_j) + \bar{\Gamma}^i{}_{ki} (\bar{\Gamma}^k - \bar{\Gamma}^{jk}{}_j)] \sqrt{\bar{\gamma}} d^3x \\ &= \oint_{\partial\Omega_1} (\bar{\Gamma}^i - \bar{\Gamma}^{ji}{}_j) d\bar{S}_i \\ &\quad + \int_{\Omega} (\bar{R} + \bar{\Gamma}^i \bar{\Gamma}^j{}_{ij} - \bar{\Gamma}^{ijk} \bar{\Gamma}_{jik}) \sqrt{\bar{\gamma}} d^3x, \end{aligned} \quad (\text{A7})$$

Similarly, the second term on the right hand side of equation (A5) yields

$$\oint_{\partial\Omega_2} \bar{D}^i \psi d\bar{S}_i = \int_{\Omega} \bar{D}^2 \psi \sqrt{\bar{\gamma}} d^3x + \oint_{\partial\Omega_1} \bar{D}^i \psi d\bar{S}_i, \quad (\text{A8})$$

where $\bar{D}^2 \equiv \bar{\gamma}^{ij} \bar{D}_i \bar{D}_j$. Collecting terms, the ADM mass (A5) can now be written

$$\begin{aligned} M &= \frac{1}{16\pi} \oint_{\partial\Omega_2} (\bar{\Gamma}^i - \bar{\Gamma}^{ji}{}_j - 8\bar{D}^i \psi) d\bar{S}_i \\ &= \frac{1}{16\pi} \int_{\Omega} (\bar{R} + \bar{\Gamma}^i \bar{\Gamma}^j{}_{ij} - \bar{\Gamma}^{ijk} \bar{\Gamma}_{jik} - 8\bar{D}^2 \psi) \sqrt{\bar{\gamma}} d^3x \\ &\quad + \frac{1}{16\pi} \oint_{\partial\Omega_1} (\bar{\Gamma}^i - \bar{\Gamma}^{ji}{}_j - 8\bar{D}^i \psi) d\bar{S}_i. \end{aligned} \quad (\text{A9})$$

We now adopt the decomposition of the BSSN formalism (Section II), in which the conformal factor is written as $\psi = e^\phi$ and the conformally related metric $\bar{\gamma}_{ij} = \gamma_{ij}$ is assumed to have determinant $\bar{\gamma} = 1$ so that $\bar{\Gamma}^j{}_{kj} = 0$. Together with the Hamiltonian constraint (24)

$$\bar{D}^2 e^\phi = \frac{e^\phi}{8} \tilde{R} + \frac{e^{5\phi}}{12} K^2 - \frac{e^{5\phi}}{8} \tilde{A}_{ij} \tilde{A}^{ij} - 2\pi e^{5\phi} \rho, \quad (\text{A10})$$

where we have included the mass-energy source $\rho \equiv n_\mu n_\nu T^{\mu\nu}$ for completeness, the ADM mass (A9) becomes

$$M = \frac{1}{16\pi} \oint_{\partial\Omega_2} (\tilde{\Gamma}^i - 8\tilde{D}^i e^\phi) d\tilde{S}_i \quad (\text{A11})$$

$$\begin{aligned} &= \frac{1}{16\pi} \int_{\Omega} d^3x \left[e^{5\phi} \left(16\pi\rho + \tilde{A}_{ij} \tilde{A}^{ij} - \frac{2}{3} K^2 \right) \right. \\ &\quad \left. - \tilde{\Gamma}^{ijk} \tilde{\Gamma}_{jik} + (1 - e^\phi) \tilde{R} \right] \\ &\quad + \frac{1}{16\pi} \oint_{\partial\Omega_1} (\tilde{\Gamma}^i - 8\tilde{D}^i e^\phi) d\tilde{S}_i, \end{aligned} \quad (\text{A12})$$

where $d\tilde{S}_i = (1/2)\epsilon_{ijk}dx^jdx^k$ since $\tilde{\gamma} = 1$.

We also note that if the conformally related metric falls off faster than inversely with r

$$\tilde{\gamma}_{ij} = \delta_{ij} + O(1/r^{1+a}), \quad a > 0 \quad (\text{A13})$$

(compare [48]), the first term in equation (A5) vanishes and the mass integral reduces to

$$\begin{aligned} M &= -\frac{1}{2\pi} \oint_{\partial\Omega_2} \tilde{D}^i e^\phi d\tilde{S}_i \\ &= \frac{1}{16\pi} \int_{\Omega} d^3x \left[e^{5\phi} \left(16\pi\rho + \tilde{A}_{ij}\tilde{A}^{ij} - \frac{2}{3}K^2 \right) - e^\phi \tilde{R} \right] \\ &\quad - \frac{1}{2\pi} \oint_{\partial\Omega_1} \tilde{D}^i e^\phi d\tilde{S}_i. \end{aligned} \quad (\text{A14})$$

Since the Kerr-Schild metric (26) does not satisfy the fall-off condition (A13), equation (A12) has to be used to evaluate its mass (equation (A14) would yield the incorrect result $M/3$ for the static Kerr-Schild metric). We have also found empirically that, even for metrics for which (A14) is appropriate, (A12) yields more accurate values for the mass than (A14) in dynamical evolution calculations [49].

2. ADM Angular Momentum Integration

We define the angular momentum J^i as

$$J_i = \frac{1}{8\pi} \epsilon_{ij}{}^k \oint_{\infty} x^j A^l{}_k dS_l. \quad (\text{A15})$$

(compare [50, 51]), where the indices of $\epsilon_{ij}{}^k$ are raised and lowered with the flat metric δ_{ij} . Since the integrand is evaluated at $r \rightarrow \infty$, we can replace $dS_i = e^{6\phi} d\tilde{S}_i$ and $A^i{}_j = \tilde{A}^i{}_j$ and use Gauss' law to obtain

$$8\pi J_i = \epsilon_{ij}{}^k \oint_{\partial\Omega_2} x^j e^{6\phi} \tilde{A}^l{}_k d\tilde{S}_l$$

$$= \epsilon_{ij}{}^k \oint_{\partial\Omega_1} x^j e^{6\phi} \tilde{A}^l{}_k d\tilde{S}_l + \epsilon_{ij}{}^k \int_{\Omega} (x^j e^{6\phi} \tilde{A}^l{}_k)_{,l} d^3x. \quad (\text{A16})$$

The volume integral in Eq. (A16) is

$$\begin{aligned} &\int_{\Omega} (x^j e^{6\phi} \tilde{A}^l{}_k)_{,l} d^3x \\ &= \int_{\Omega} \left[\delta^j_l e^{6\phi} \tilde{A}^l{}_k + x^j (e^{6\phi} \tilde{A}^l{}_k)_{,l} \right] d^3x \\ &= \int_{\Omega} \left[e^{6\phi} \tilde{A}^j{}_k + x^j \tilde{D}_l (e^{6\phi} \tilde{A}^l{}_k) + e^{6\phi} x^j \tilde{\Gamma}^n{}_{kl} \tilde{A}^l{}_n \right] d^3x \\ &= \int_{\Omega} \left[e^{6\phi} \tilde{A}^j{}_k + x^j \tilde{D}_l (e^{6\phi} \tilde{A}^l{}_k) - \frac{1}{2} e^{6\phi} x^j \tilde{A}_{ln} \tilde{\gamma}^{ln}{}_{,k} \right] d^3x \end{aligned} \quad (\text{A17})$$

where we have used $\tilde{\gamma} = 1$. With the momentum constraint,

$$\tilde{D}_j (e^{6\phi} \tilde{A}^j{}_i) = e^{6\phi} \left(\frac{2}{3} \tilde{D}_i K + 8\pi s_i \right), \quad (\text{A18})$$

where we have included the momentum density $s_i \equiv \gamma_{i\mu} n_\nu T^{\mu\nu}$ for completeness, the volume integral (A18) can be rewritten

$$J_i = \frac{1}{8\pi} \epsilon_{ij}{}^k \oint_{\partial\Omega_2} e^{6\phi} x^j \tilde{A}^l{}_k d\tilde{S}_l \quad (\text{A19})$$

$$\begin{aligned} &= \frac{1}{8\pi} \epsilon_{ij}{}^k \int_{\Omega} \left[\tilde{A}^j{}_k + \frac{2}{3} x^j \tilde{D}_k K \right. \\ &\quad \left. - \frac{1}{2} x^j \tilde{A}_{ln} \partial_k \tilde{\gamma}^{ln} + 8\pi x^j s_k \right] d^3x \\ &\quad + \frac{1}{8\pi} \epsilon_{ij}{}^k \oint_{\partial\Omega_1} e^{6\phi} x^j \tilde{A}^l{}_k d\tilde{S}_l. \end{aligned} \quad (\text{A20})$$

This expression is equivalent to Eq. (2.25) of [8]. Note that the first term does not vanish identically, since indices of ϵ_{ijn} are raised with δ_{ij} while indices of \tilde{A}^{jn} are lowered with $\tilde{\gamma}_{ij}$.

-
- [1] R. Arnowitt, S. Deser and C. W. Misner, in *Gravitation: An Introduction to Current Research*, edited by L. Witten (Wiley, New York, 1962).
 - [2] C. Bona *et al*, Phys. Rev. Lett. **75**, 600 (1995).
 - [3] T. W. Baumgarte and S. L. Shapiro, Phys. Rev. D **59**, 024007 (1999).
 - [4] A. Anderson and J. W. York, Jr., Phys. Rev. Lett. **82**, 4384 (1999).
 - [5] O. Reula, Living Rev. Rel. **1**, 3 (1998).
 - [6] M. Shibata and T. Nakamura, Phys. Rev. D **52**, 5428 (1995).
 - [7] T. W. Baumgarte, S. A. Hughes, and S. L. Shapiro, Phys. Rev. D **60** 087501 (1999).
 - [8] M. Shibata, Phys. Rev. D **60**, 104052 (1999).
 - [9] M. Shibata and K. Uryu, Phys. Rev. D **61**, 064001 (2000).
 - [10] M. Shibata, T. W. Baumgarte, and S. L. Shapiro, Phys. Rev. D **61**, 044012 (2000).
 - [11] M. Alcubierre *et al*, Phys. Rev. D **61**, 041501 (2000).
 - [12] M. Alcubierre *et al*, Phys. Rev. D **62**, 124011 (2000).
 - [13] L. Smarr and J. York, Phys. Rev. D **17**, 2529 (1978).
 - [14] D. Eardley and L. Smarr, Phys. Rev. D **19**, 2239 (1979).
 - [15] J. M. Bardeen and T. Piran, Phys. Rep. **196**, 205 (1983).
 - [16] L.I. Petrich, S.L. Shapiro, and S.A. Teukolsky, Phys. Rev. D **31**, 2459 (1985); **33**, 2100 (1986).
 - [17] W.G. Unruh, as cited in [18] (1984).
 - [18] J. Thornburg, Class. Quantum Grav. **4**, 1119 (1987).
 - [19] E. Seidel and W.-M. Suen, Phys. Rev. Lett. **69**, 1845 (1992).
 - [20] J. Thornburg, PhD. thesis, Univ. of British Columbia, Vancouver, British Columbia, 1993.
 - [21] P. Anninos *et al*, Phys. Rev. D **51**, 5562 (1995).
 - [22] M. A. Scheel, S. L. Shapiro and S. A. Teukolsky, Phys.

- Rev. D **51**, 4208 (1995).
- [23] S. Brandt *et al*, Phys. Rev. Lett. **85**, 5496 (2000).
 - [24] R. A. Matzner, M. F. Huq, and D. Shoemaker, Phys. Rev. D **59**, 024015 (1999).
 - [25] N. T. Bishop *et al*, Phys. Rev. D **57**, 6113 (1998).
 - [26] P. Marronetti and R. A. Matzner, Phys. Rev. Lett. **85**, 5500 (2000).
 - [27] O. Sarbarch, M. Tiglio, and J. Pullin, Phys. Rev. D **65**, 064026 (2002).
 - [28] H. P. Pfeiffer, G. B. Cook, and S. A. Teukolsky, gr-qc/0203085 (2002).
 - [29] M. Alcubierre and B. Brügmann, Phys. Rev. D **63**, 104006 (2001).
 - [30] M. A. Scheel, talk given at the ITP Miniprogram “Colliding Black Holes: Mathematical Issues in Numerical Relativity”, January 10 – 28, 2000.
 - [31] P. Laguna and D. Shoemaker, gr-qc/0202105 (2002).
 - [32] L. Lindblom and M. Scheel, gr-qc/0206035 (2002).
 - [33] L. E. Kidder, M. A. Scheel, and S. A. Teukolsky, Phys. Rev. D **64**, 064017 (2001).
 - [34] S. Detweiler, Phys. Rev. D **35**, 1095 (1987).
 - [35] G. Yoneda and H. Shinkai, Phys. Rev. D **63**, 124019 (2001).
 - [36] B. Kelly, P. Laguna, K. Lockitch, J. Pullin, E. Schnetter, D. Shoemaker, and M. Tiglio, Phys. Rev. D **64**, 084013 (2001).
 - [37] G. Yoneda and H. Shinkai, gr-qc/0204002.
 - [38] A. M. Knapp, E. J. Walker, T. W. Baumgarte, Phys. Rev. D **65**, 064031 (2002).
 - [39] S. Chandrasekhar, *The Mathematical Theory of Black Holes* (Oxford University Press, New York, 1992).
 - [40] A. E. Eddington, Nature **113**, 192 (1924); D. Finkelstein, Phys. Rev. **110**, 965 (1958).
 - [41] S. Teukolsky, Phys. Rev. D **61**, 087501 (2000).
 - [42] C. Bona *et al.*, Phys. Rev. Lett. **75**, 600 (1995).
 - [43] A. Arbona *et al.*, Phys. Rev. D **60**, 104014 (1999).
 - [44] M. Alcubierre *et al.*, Phys. Rev. D **62**, 044034 (2000).
 - [45] The Gamma-driver condition (equations (45) and (49)) is a parabolic equation for the shift, $\partial_t \beta^i \sim \lambda \tilde{\gamma}^{jk} \beta^i{}_{,jk}$. Accordingly, stability requires that we set $\lambda \propto (\Delta x)^2 / \Delta t \propto \Delta x$ when $\Delta x / \Delta t$ is fixed by a hyperbolic Courant condition.
 - [46] H.-J. Yo, T. W. Baumgarte, and S. L. Shapiro, Phys. Rev. D **64**, 124011 (2001).
 - [47] T. W. Baumgarte, *et al.*, Phys. Rev. D **54**, 4849 (1996).
 - [48] N. Ó Murchadha and J. W. York, Jr., Phys. Rev. D **10**, 2345, (1974).
 - [49] M. D. Duez, T. W. Baumgarte, P. Marronetti, and S. L. Shapiro, in preparation, 2002.
 - [50] J. W. York, Jr., in *Sources of Gravitational Radiation*, edited by L.L. Smarr (Cambridge Univ. Press, Cambridge, 1979).
 - [51] J. M. Bowen and J. W. York, Jr., Phys. Rev. D **21** 2047 (1980).